Journal of Materials Science and Chemical Engineering, 2024, 12, 88-107
https://www.scirp.org/journal/msce
ISSN Online: 2327-6053
ISSN Print: 2327-6045

Synthesis, Characterization, and Evaluation Non-Stoichiometric of Copper Ferrite Nanoparticles in Disinfestation and Adsorption Efficiency for Organic Dye: Isotherms, Thermodynamics, and Kinetic Studies

Noor Aati Alrishi[1*], Atikah Musa Alnahari[1], Amal Mozarei Ibrahim[2], Saedah Rwede Almhyawi[1], Mai Hammad Alsuwat[1]

[1]Department of Chemistry, College of Science, University of Jeddah, Jeddah, Saudi Arabia
[2]Physical Chemistry Department, Advanced Materials Technology and Mineral Resources Research Institute, National Research Center, Cairo, Egypt
Email: *Noorarishi@outlook.com, Atkahm1993@gmail.com, amozarei@gmail.com, sral-mhyawi@uj.edu.sa, maialsuwat@gmail.com

How to cite this paper: Alrishi, N.A., Alnahari, A.M., Ibrahim, A.M., Almhyawi, S.R. and Alsuwat, M.H. (2024) Synthesis, Characterization, and Evaluation Non-Stoichiometric of Copper Ferrite Nanoparticles in Disinfestation and Adsorption Efficiency for Organic Dye: Isotherms, Thermodynamics, and Kinetic Studies. *Journal of Materials Science and Chemical Engineering*, **12**, 88-107.
https://doi.org/10.4236/msce.2024.1212007

Received: November 16, 2024
Accepted: December 20, 2024
Published: December 23, 2024

Abstract

Ferrite nanoparticles (FNPs) have attracted considerable attention due to their diverse applications in wastewater treatment. This study focused on synthesizing non-stoichiometric copper ferrite magnetic nanoparticles (CuFNPs) through co-precipitation and microwave methods. The synthesized adsorbents were characterized using techniques such as X-ray diffraction (XRD), vibration sample magnetometry (VSM), and scanning electron microscopy (SEM). XRD analysis revealed crystallite sizes ranging from 24 to 31 nm for all samples. Furthermore, adsorption experiments were performed to investigate the impacts of several factors, including dye concentration, contact time, adsorbent dosage, and pH, on the removal efficiency of Alizarin Yellow R (AYR) dye. The CuFNPs (5) sample achieved a maximum removal efficiency of 98.90% at a dye concentration of 50 ppm, pH 2, and an equilibrium time of 90 minutes. The kinetic investigation demonstrated that the adsorption of AYR dye onto the nanoparticles adhered to a pseudo-second-order (PSO) model. The adsorption equilibrium data were most accurately described by the Langmuir isotherm model, although the Freundlich model was also evaluated. The CuFNPs (4) sample showed superparamagnetic behavior with a

saturation magnetization value of 58.28 emu/g. The antibacterial activity of the synthesized CuFNPs was evaluated against four bacterial strains, including gram-positive, gram-negative, and pathogenic fungal yeast. Results showed that the CuFNPs (5) sample demonstrated significant effectiveness against both gram-negative bacteria (*E. coli*, *P. aeruginosa*) and gram-positive bacteria (*S. aureus*, *B. cereus*), as well as the pathogenic fungal yeast *C. albicans*.

Keywords

Copper Ferrite Nanoparticles, Alizarine Yellow R Dye, Adsorption Isotherms, Antibacterial Activities

1. Introduction

Water is essential for all biological entities, including humans, for food production and economic development. It is a critical natural resource, covering approximately 75% of our planet and the Earth's crust [1]. However, the availability of clean water is compromised by various natural and human-induced processes. Each year, contaminated water leads to 4 million cases of diarrheal diseases and 2.2 million deaths [2]. As a result, water pollution is the most challenging environmental problem facing humanity [3]. Water contamination refers to the introduction of chemicals and substances that exceed the safe absorption threshold, posing harm to living beings [4]. Among many pollutants, organic dyes are major contributors due to their intricate molecular composition [5]. Most organic dyes are carcinogenic and threaten human health and ecosystems [6]. Therefore, there is an urgent need for an economical and effective method to remove these dyes before they are discharged into ecosystems. Recently, nanotechnology has shown that nanomaterials can effectively address water pollution issues. Specifically, experts are increasingly investigating the use of iron nanoparticles to remediate groundwater polluted by industrial waste. These nanoparticles can help remove harmful and carcinogenic organic pollutants from contaminated water [7]. Nanostructured ferrites are essential materials in technology, commonly used in transducers, sensors, ferrofluids, and biochemical applications [8]. Spinel ferrites (SFs), which are magnetic substances that are thermally stable, are represented as MFe_2O_4 (where M denotes a metallic cation) and have a wide range of applications [9]. SFs have extraordinary physical and chemical properties, excellent magnetic properties, and a high specific surface area, resulting in many surface-active sites [10]. Removing contaminants from water requires exceptional adsorption efficiency and rapid kinetics, making SFs adsorption materials the preferred option [10]. The surface chemical composition, magnetic characteristics, and morphological arrangements of ferrite nanomaterials are determined by the synthesis approaches and initial ingredients employed [11]. As a result, nanostructured copper-based ferrite substances can serve as photocatalysts and adsorbers for purifying and treating water [12]. Numerous studies have evaluated the effectiveness of

different types of magnetic nanoparticles, including ferrites, for dye removal [13]-[16]. The microwave-hydrothermal route's efficiency for magnetic nanoferrite (MFe_2O_4, M = Co, Ni) was studied by Mishra *et al*. [13]. In this study, the obtained magnetic nanoferrite was used to remove Bromo-phenol Blue (BRB) and Eriochrome Black T (EBT) dyes from water-based solutions [13]. Moreover, the investigation of Cu-substituted ferrite nanoparticles for their effectiveness in eliminating Alizarin Red S (ARS) dye, as well as their reusability, has been reported [14]. In another report, Zaharieva *et al*. [16] studied the efficiency of copper ferrite for the photocatalytic treatment of wastewater containing organic dyes using a combination of thermal treatment, mechanochemical activation, and co-precipitation. To date, various methodologies have been implemented to synthesize ferrite nanostructures, including co-precipitation [17], conventional chemical methods [18], microwave combustion [10], and the sol-gel method [19]. Among the methods for synthesizing nanoscale ferrites, the microwave technique is straightforward, quick, cost-effective, and sustainable [20]. However, there is limited literature on how the preparation method influences removal efficiency and biological activity. This study aimed to prepare non-stoichiometric copper ferrite magnetic nanoparticles (CuFNPs) using co-precipitation and a rapid microwave method and compare their adsorption efficiency with Alizarine Yellow R (AYR) dye. Various experimental controls were adjusted, and the resulting data were used to demonstrate adsorption isotherm models, thermodynamic, and kinetic parameters. Furthermore, the biological activities of the prepared CuFNPs were examined against pathogenic yeast and bacterial strains (both gram-positive and gram-negative).

2. Materials and Methods

2.1. Materials

Materials used in this study include ferrous sulphate-heptahydrate ($FeSO_4{\cdot}7H_2O$), copper (II) acetate $Cu(CH_3COO)_2$, ammonium hydroxide 30% (NH_4OH), sodium hydroxide (NH_4OH), ferric chloride ($FeCl_3{\cdot}6H_2O$), ethylene glycol $(CH_2OH)_2$, hydrochloric acid (HCl), and AYR dye. All chemicals and materials used in this study were acquired from Sigma Aldrich Company.

2.2. Preparation of Copper Ferrite Nanoparticles (Co-Precipitation) Method

Prepared ferrite nanoparticles (FNPs) with different molar ratios of (CuFNPs). $FeSO_4{\cdot}7H_2O$, $FeCl_3{\cdot}H_2O$, and Cu $(CH_3COO)_2$ were used in varying molar ratios of Cu^{2+} so that the FNPs could be represented as $(Cu_xFe_{1-x})O{\cdot}Fe_2O_3$, where divalent Copper replaces Fe^{2+}. The co-precipitation process involved adding a 30% ammonium hydroxide solution dropwise while continuously stirring to reach a pH of 10. The reaction was conducted at 50˚C, after which the mixture was allowed to cool to ambient temperature. Through centrifugation, the particulates were separated, rinsed multiple times with deionized water, and subsequently treated with ethyl

alcohol. In the final stage, they were desiccated in a hot air oven at 80˚C for 12 hours. The obtained CuFNPs samples were denoted as CuFNPs (0), CuFNPs (1), CuFNPs (2), CuFNPs (3), and CuFNPs (4), corresponding to Fe_3O_4, $(Cu_{0.25}Fe_{0.75})O{\cdot}Fe_2O_3$, $(Cu_{0.5}Fe_{0.5})O{\cdot}Fe_2O_3$, $(Cu_{0.75}Fe_{0.25})O{\cdot}Fe_2O_3$, and $CuFe_2O_4$, respectively.

2.3. Preparation of Copper Ferrite Nanoparticles (Microwave Technique)

Copper ferrite nanoparticles were synthesized using a microwave technique. In this method, 5.4 g of ferric chloride ($FeCl_3{\cdot}H_2O$) and 1.81 g of copper (II) acetate $Cu(CH_3COO)_2$ were mixed with ethylene glycol at a solid-to-liquid ratio of 1:10. An enclosed Teflon tube contained the precursor mixture, which was then exposed to microwave radiation for 2 minutes at 700 W in a 2.45 GHz multimode cavity. This design took advantage of ethylene glycol's high dielectric loss, allowing it to heat rapidly during microwave irradiation. The resulting solid was filtered, rinsed with ethanol, and desiccated. The obtained samples are denoted as CuFNPs (5).

2.4. Characterization

The synthesized nanoparticles were analyzed using an X-ray diffractometer (XRD) (Shimadzu-7000, USA) for phase analysis and crystallite size measurement. Dye concentrations during the photocatalytic process were monitored using a UV-visible spectrophotometer (UV-1800 Shimadzu) with a resolution of 1 nm. The morphology and structure of the samples were examined using a scanning electron microscope (SEM; JEOL JSM-7600F). A Lake Shore Model 7410 (USA) Vibrating Sample Magnetometer (VSM) was used to explore the magnetic features.

2.5. Evaluation Study for Removal of Alizarine Yellow R (AYR) Dye

2.5.1. Preparation of AYR Dye Solution

The concentration of a stock solution was 1000 mg/L, achieved by dissolving 1 g of AYR dye in 1 L of distilled water. This solution was kept in a volumetric flask for preparing diluted AYR dye solutions. The Shimadzu UV-1800 UV-visible spectrophotometer was used to determine dye concentrations before and after adsorption. The concentrations were measured by absorbance within a wavelength range of 200 to 500 nm for AYR dye. Calibration curves were constructed using solutions of 25, 50, 75, and 100 mg/L for equilibrium and kinetic investigations.

2.5.2. Adsorption Study

In a typical batch adsorption experiment, 10 g of adsorbent was combined with 20 mL of 50 mg/L dye. The mixture was stirred at 25˚C throughout the experiment. The pH was initially adjusted to the desired value using small amounts of NaOH and HCl (0.1 mol/L). Experiments used 20 mL of 50 mg/L dye at varying pH levels (2 to 10). Different time intervals (15 to 150 minutes) were used to study the impact of contact time on adsorption. The effect of the initial concentration

of AYR dye was examined using dye solutions of 25, 50, 75, and 100 mg/L with 10 mg of CuFNPs. Additionally, the effect of adsorbent mass (10, 15, 20, and 40 mg) on dye removal was studied by interacting with 20 mL of 50 mg/L dye at ambient temperature. The following equation was used to calculate the removal percentage (R%) of AYR dye (1) [21]:

$$R(\%) = \frac{C_0 - C}{C_0} \times 100\% , \quad (1)$$

where C_0 and C denote the dye concentration before and after a catalyst degrades it.

2.5.3. Antibacterial Activity Study

Using nutrient agar plates, qualitative evaluations were conducted [22]. A spore suspension of the pathogenic isolates was generated and calibrated to a concentration of approximately 0.5 McFarland standard (1.5×10^8 cells/ml). Each plate contained 20.0 mL of sterile nutrient agar medium, and 25.0 µL of yeast and bacterial preparations were inoculated into it. After the medium cooled and solidified, 100 µL of the prepared samples were inserted into pre-formed wells on the agar plates, which had a diameter of 0.9 mm. Incubation was conducted at 37˚C for 24 hours after the inoculated dishes were refrigerated for one hour. The samples' efficacy against the targeted bacteria was assessed by measuring their zones of inhibition (ZI) in millimeters [23] [24].

3. Results and Discussion

3.1. X-Ray Diffraction Study

XRD was used to determine the crystallite phase and calculate the crystallite size. The XRD pattern for the samples from CuFNPs (0) to CuFNPs (5) is shown in **Figure 1**. According to the XRD figure, the pattern for the CuFNPs (0) sample aligns with JCPDS (79-0417) indicating a pure magnetite phase with 2θ = 29.75˚, 32.15˚, 35.75˚, 43.3˚, 57.1˚, 60.95˚, and 62.95˚. The XRD pattern of the CuFNPs (1) sample shows an amorphous nature and a pattern corresponding to magnetite, making it difficult to identify any peaks belonging to copper ferrite. This could be due to the small amount of ferrite and the amorphous nature of the pattern. The diffractogram for the CuFNPs (2) sample shows a pattern representing Fe_3O_4 and $CuFe_2O_4$, in agreement with JCPDS (79-0417) and (34.0425), respectively. Peaks for Fe_3O_4 are at 2θ = 29.6˚, 32.8˚, 34.4˚, and 61.1˚, while those for Cu Fe_2O_4 are at 2θ = 43.7˚, 35.15˚, 58.15˚, and 70.05˚. The CuFNPs (3) sample shows an amorphous nature with a pattern mainly assigned to copper ferrite at 2θ = 35.4˚, 43.25˚, 56.9˚, and 69.5˚. The few peaks belong to magnetite at 2θ = 32.8˚ and 61.7˚. On the other hand, the CuFNPs (4) sample represents the XRD pattern in agreement with JCPDS card number 34-0425. The assigned pattern includes peaks at 2θ = 16.25˚, 26.7˚, 35.15˚, 38.75˚, 43˚, 55.9˚ and 48.5˚. The CuFNPs (5) sample showed a well-crystalline pattern with peaks assigned at 2θ = 16.75˚, 22˚, 26.7˚, 28.9˚, 30.65˚, 32.6˚, 34.05˚, 35.45˚, 40.85˚, 43.05˚, 44.8˚, 49.1˚, 54.45˚, 57.4˚, and 93.9˚. Remarkably, the sample prepared using

microwave assistance exhibited a crystalline structure, with its crystallite size remaining relatively unchanged and comparable to that of the traditionally prepared sample. Comparing the XRD results of the as-prepared non-stoichiometric copper ferrite reveals that, despite the smaller crystallite size of the microwave-assisted sample compared to traditionally prepared samples, it exhibits a more defined crystallite pattern. This may be attributed to the shorter reaction time in the microwave process compared to the traditional method. However, the thermal energy involved in the microwave preparation method is much greater than that in the traditional co-precipitation method. Therefore, the microwave-prepared sample possesses sufficient thermal energy for good crystallinity, but the crystallization time is too brief to allow for an increase in crystallite size.

Scherer's equation was applied to analyze the crystallite size of the samples:

$$L = \frac{0.89\lambda}{\beta \cos\theta}, \tag{2}$$

where the diffraction peak's full width at half maximum (FWHM) is designated by β, the crystallite size by L, the X-ray wavelength is 0.154 nm, and the Bragg peak position by θ.

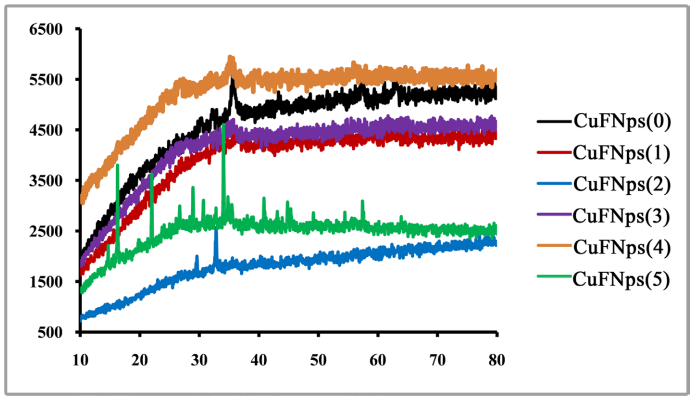

Figure 1. XRD-pattern for the samples from CuFNPs (0) to CuFNPs (5).

3.2. Morphological Analysis

The morphology of samples was investigated using SEM. The SEM of synthesized CuFNPs (0) **Figure 2(a)** showed agglomerated nanoparticles with some degree of homogeneity. The particle size in CuFNPs (1) appeared smaller than that of sample CuFNPs (0) (**Figure 2(b)**). This is likely due to the initial formation of the ferrite phase, which reduces agglomeration. Samples CuFNPs (2) and CuFNPs (3) (**Figure 2(c)**, **Figure 2(d)**) exhibited a similar trend of non-magnetic particle aggregation. Sample CuFNPs (4) **Figure 2(e)** showed pure $CuFe_2O_4$ agglomeration from nano-sized particles and had a lower degree of homogeneity than the other samples. Sample CuFNPs (5) is shown in **Figure 2(f)**. From the image, it is clear that the $CuFe_2O_4$ particle size is much smaller than in samples prepared by the traditional co-precipitation method. This reduction in particle size may be due to

the shorter preparation time, which limits the growth of crystallites and particles. Additionally, the solvent used (ethylene glycol) reduces particle aggregation during precipitation. The high thermal energy from the microwave-assisted technique also enhances the crystallinity of the produced $CuFe_2O_4$.

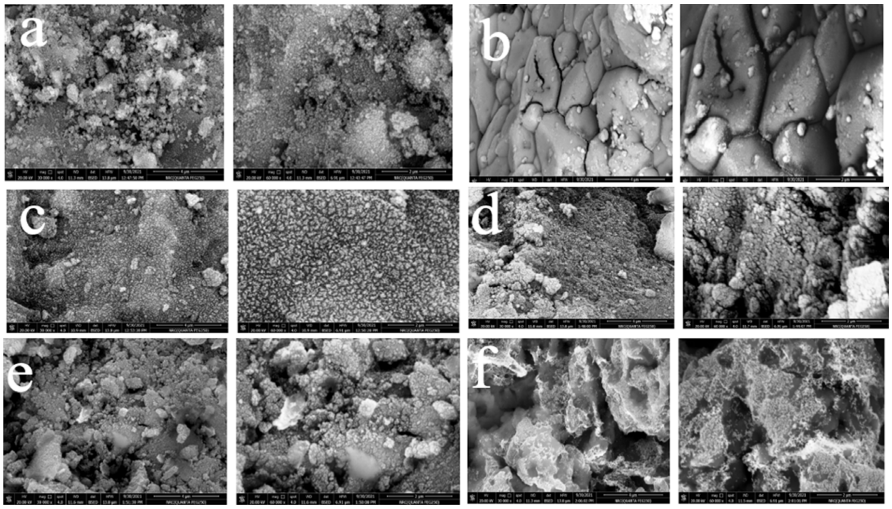

Figure 2. SEM images of (a) CuFNPs (0), (b) CuFNPs (1), (c) CuFNPs (2), (d) CuFNPs (3), (e) CuFNPs (4), and (f) CuFNPs (5).

3.3. Vibrating Sample Magnetometer (VSM)

The assessment of magnetic materials requires examining their magnetic characteristics. This study investigated the relationship between the intensity of the applied magnetic field (H) and magnetization (M) for various samples. The hysteresis loop of the sample CuFNPs (0), shown in **Figure 3(a)**, which contains no copper and is essentially Fe_3O_4, exhibited a saturation magnetization (Ms) of 58.28 emu/g and a coercivity of 15.26 Hci. The Ms value aligns with existing literature, although the coercivity was notably higher than reported in the literature [25]. Given that iron oxide behaves as a superparamagnetic material at room temperature with particle sizes below 10 nm, the larger crystallite size of Fe_3O_4 in this study resulted in non-superparamagnetic behavior [26]. As copper ions were introduced into the ferrite structure, significant changes were observed. For CuFNPs (1) with 25% copper, as shown in **Figure 3(b)**, the Ms dropped to 6.8 emu/g due to the introduction of Cu^{2+} ions, leading to surface inhomogeneity and an anisotropic layer, while coercivity decreased to 7.24 Hci [27]. For CuFNPs (2) with 50% copper, **Figure 3(c)** shows the hysteresis loop indicating superparamagnetic properties, with a decrease in saturation magnetization to 0.75 Hci, attributed to reduced particle size. This trend continued with CuFNPs (3) **Figure 3(d)**, containing 75% copper, which maintained superparamagnetic characteristics, showing an Ms of 28.9 emu/g and a coercivity of 0.74 Hci. The pure $CuFe_2O_4$ sample, CuFNPs (4), exhibited similar linear behavior in **Figure 3(e)**, with an Ms of 41.8 emu/g, which is smaller than that cited in previous literature (33.3 emu/g) [28] [29]. Also, it showed increased coercivity of 0.52 Hci, linked to reduced particle size. The

microwave-assisted preparation of pure $CuFe_2O_4$ (CuFNPs (5), **Figure 3(f)** produced an Ms of 53.75 emu/g and a coercivity of 0.91 Hci, slightly lower than conventionally prepared samples, possibly due to the formation of small metallic clusters of Cu and Fe from rapid reactions [30]. Overall, the variations in saturation magnetization across different samples were primarily due to changes in particle size, except for the microwave-assisted sample, which exhibited unique properties. Coercivity generally increased with decreasing particle size. The magnetic parameters measured were close to those reported for bulk $CuFe_2O_4$, attributed to crystallite sizes near the single-domain range ($CuFe_2O_4$ 24 m^2) [31].

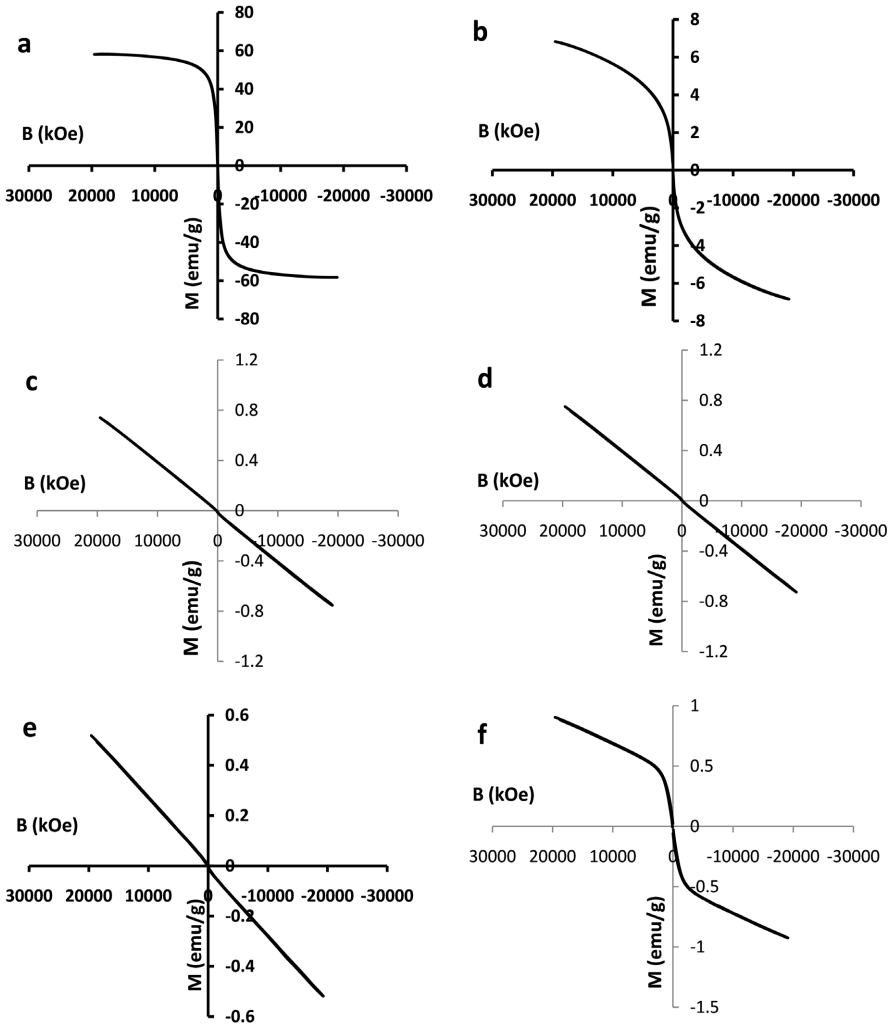

Figure 3. VSM images of (a) CuFNPs (0), (b) CuFNPs (1), (c) CuFNPs (2), (d) CuFNPs (3), (e) CuFNPs (4), and (f) CuFNPs (5).

3.4. Adsorption Studies

To evaluate the adsorption efficiency of the CuFNPs adsorbent samples, preliminary experiments were conducted under varying parameters, including contact time, adsorbent mass, initial adsorbate concentration, and pH, to determine the optimal conditions for eliminating AYR dye from water-based solutions.

3.4.1. Effect of Contact Time

The contact time between pollutants and sorbent material is an important factor affecting the efficiency of dye removal. Therefore, a series of experiments was conducted at various contact times of the dye solution. The experimental parameters were set at a pH of 6.7, an adsorbent dosage of 10 mg, and 20 mL of AYR dye at a concentration of 50 ppm, all conducted at ambient temperature. During the initial phase of the adsorption process (0 - 15 minutes), the apparent rate constant of the reaction increased with extended contact time, attributed to the abundance of active sites on the surfaces of the nanoparticles available for AYR dye adsorption (see **Figure 4**). For comparison, a test for AYR dye adsorption on different molar ratios of nanocrystalline copper ferrite was conducted under the same conditions at different contact times. The results indicate that the removal percentage increases with a higher molar ratio of copper ferrite and longer contact time. The optimum contact time after 150 minutes for maximum removal for the six samples from CuFNPs (0) to CuFNPs (5) was 37.28%, 43.44%, 63.41%, 80.91%, 94.03%, 98.89%, respectively. On the other hand, the increase in removal efficiency for AYR can be attributed to the higher molar ratios of copper ferrite. This is because Cu^{2+} ions play a key role in enhancing the performance of the samples in removing the dye. By contrast, although the two samples, CuFNPs (4) and CuFNPs (5), contain the same molar ratios of copper ferrite, we noticed a higher removal efficiency for sample CuFNPs (5), which was prepared by microwave. The rapid transformation by microwaves helps form nanoparticles with smaller sizes and a high surface area. Hence, many active sites are created on the surface of CuFNPs (5).

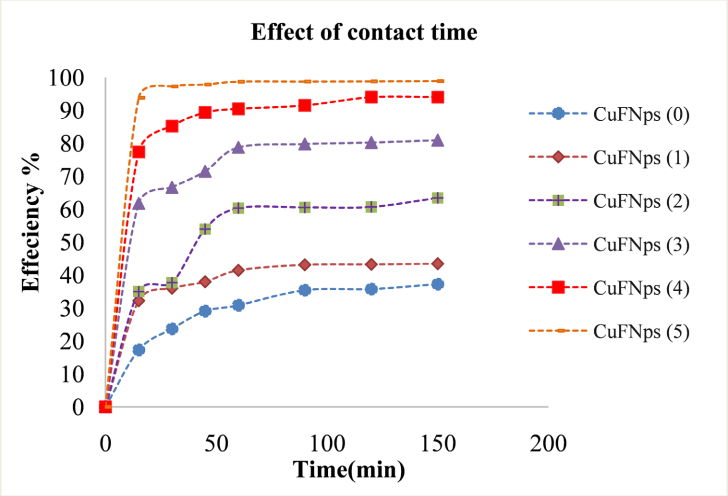

Figure 4. Graph of the effect of contact time on AYR dye removal onto CuFNPs samples.

3.4.2. Effect of the Adsorbent Mass

A series of experiments were conducted using various adsorbent masses added to the dye solution, as illustrated in **Figure 5**. The experimental settings included a pH of 6.7, a dye concentration of 50 ppm in 20 mL, and an initial temperature of room temperature for 90 minutes. The adsorbent mass ranged from 10 to 40 mg.

The findings indicated that increasing the adsorbent mass significantly improved removal efficiency by providing more active sites for AYR particle binding. The data showed that the adsorption percentage of AYR dye increased with higher quantities of CuFNPs. The maximum removal efficiencies for the six samples, from CuFNPs (0) to CuFNPs (5) at a dosage of 40 mg, were about 73.2%, 86.09%, 87.65%, 89.45%, 95.84%, and 98.85%, respectively. An adsorbent weight of 10 mg was chosen as the optimum weight for studying other factors due to the minor increase in removal efficiency with doses above 10 mg.

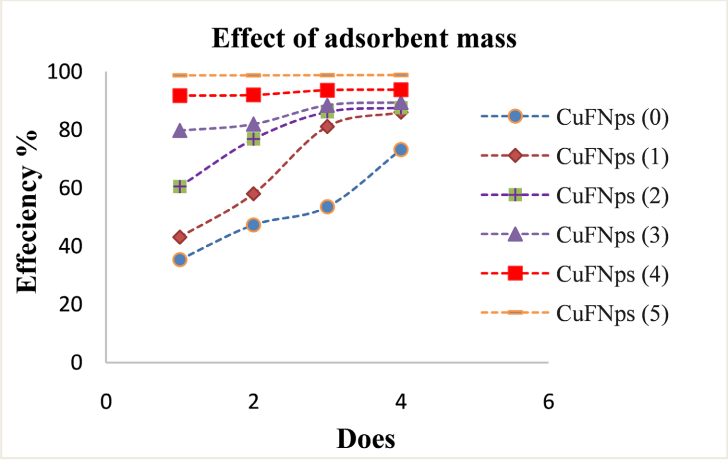

Figure 5. Graph illustrating the impact of adsorbent mass on AYR dye removal using CuFNPs samples.

3.4.3. Effect of Adsorbent Concentration

AYR dye solutions with concentrations between 25 and 100 mg/L were prepared to study the impact of initial dye amounts on removal efficiency. The experiments were conducted at a pH of 6.7, with an adsorbent mass of 10 mg and a dye concentration of 50 ppm in 20 mL, at room temperature for 90 minutes. Figure 6 shows that the optimal contact concentration was 25 ppm at equilibrium time for maximum removal. However, the removal percentage declined as the initial dye concentration increased. For example, the removal efficiency for CuFNPs (5) decreased gradually from 99% to 95.17% as the initial dye concentration increased from 25 to 100 ppm. It is evident that the quantity of dye adsorbed decreases as the initial dye content increases. Higher initial dye concentrations result in lower percentages of dye being adsorbed due to the increased competition for active sites on the CuFNPs surface, eventually leading to saturation of these sites.

3.4.4. Effect of pH

The impact of pH on AYR removal was examined, with values ranging from 2 to 10, as illustrated in Figure 7. The removal efficiency increases in acidic conditions, with a pH decrease from 6.8 to 2. The maximum removal at pH 2 for the six samples from CuFNPs (0) to CuFNPs (5) was approximately 79.30%, 81.35%, 86.15%, 88.96%, 93.42%, and 98.90%, respectively. This is because the ionized CuFNPs

functional groups form strong electrostatic contacts with the negatively charged anionic dye molecules and the positively charged CuFNPs surface. On the other hand, removal effectiveness dropped for the six samples from CuFNPs (0) to CuFNPs (5) to about 20.24%, 31.31%, 49.89%, 59.86%, 80.03%, and 96.20%, respectively, at pH 10. This decrease at basic pH values occurs because anions compete with excess OH ions for adsorption sites on CuFNPs, destabilizing the anionic dyes.

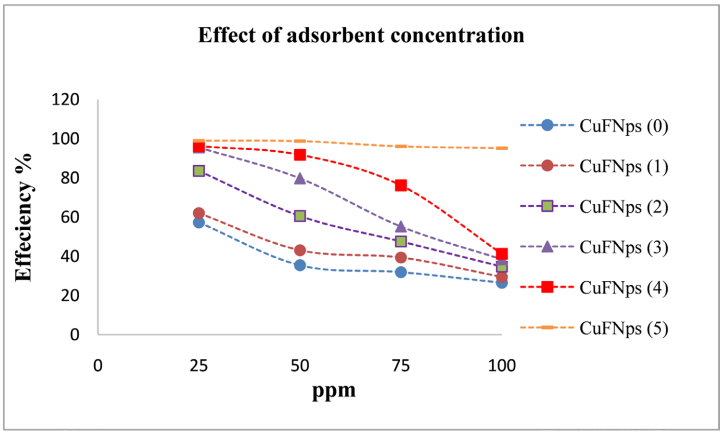

Figure 6. Graph of the impact of adsorbent concentration on AYR dye removal onto CuFNPs.

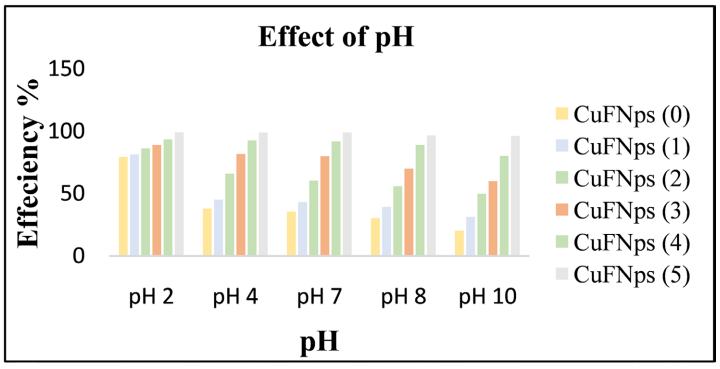

Figure 7. Graph of the impact of pH on AYR dye removal using CuFNPs samples.

3.5. Kinetic Study

The pseudo-first-order (PFO) and pseudo-second-order (PSO) chemisorption models are frequently used to analyze the kinetics of aqueous pollutant removal with various adsorbents [32]. Adsorption kinetics are important as they provide insights into the adsorption mechanism, which is crucial for enhancing process efficiency [33]. In this study, adsorption data for CuFNPs at different time intervals were examined using the PFO and PSO kinetic models. The adsorption rate is a critical factor when selecting an adsorbent, as it needs to exhibit both high adsorption capacity and rapid adsorption rate [34].

3.5.1. Lagergren Pseudo First Order

The principle of the PFO kinetic approach is that the rate of variation in solute

absorption over time is directly correlated to the difference between the concentration at equilibrium and the quantity of solute adsorbed at that time [35].

The first-order kinetics, as postulated by Lagergren, is denoted by the subsequent equation (3) [36]:

$$\ln\left(q_e - q_t\right) = \ln q_e - K_1 t \,. \tag{3}$$

The values of q_e and K_1 can be obtained using linear regression of experimental data shown as $\ln(q_e - q_t)$ vs time t. In this context, q_e and q_t denote the adsorption amounts per unit mass at equilibrium and at any specific time, respectively, where K_1 signifies a PFO rate constant. The equilibrium adsorption capacity q_e and the PFO rate constant K_1 can be experimentally measured from the intercept and slope derived by graphing $\ln(q_e - q_t)$ versus time. **Figure 8(a)** demonstrates that the PFO model does not align well with the kinetic data, as shown by the low regression coefficient R^2 presented in **Table 1**.

3.5.2. Pseudo Second Order

The PSO model principle takes into account the different phases during adsorption processes, effectively explaining the majority of sorption systems. PSO characterizes the adsorption process as chemisorption and can be represented as [37]:

$$\frac{\mathrm{d}(AC)_t}{\mathrm{d}t} = K\left[(AC)_0 - (AC)_t\right]^2, \tag{4}$$

where $(AC)_t$ represents the number of active sites occupied on the CuFNPs at any time, and $(AC)_0$ is the number of active sites available on the adsorbent surface.

The kinetic rate equations can thus be rewritten as follows:

$$\frac{\mathrm{d}q}{\mathrm{d}t} = K_2\left(q_e - q\right)^2, \tag{5}$$

In this context, k_2 represents the rate of sorption (g/mg min), while q_e (mg/g) and q (mg/g) denote the amounts of dye adsorbed at equilibrium and at any time, respectively. Separating Equation (5) gives:

$$\frac{\mathrm{d}q}{\left(q_e - q\right)^2} = K_2 \mathrm{d}t \,. \tag{6}$$

Integrating Equation (6) for the boundary conditions $t = 0$ to $t = t$ and $q = 0$ to $q = q$ gives:

$$\frac{1}{q_e - q} = \frac{1}{q_e} + K_2 t \,, \tag{7}$$

which is the integrated rate law for pseudo-second reaction.

These values can be obtained by plotting t/q_t against t, as shown in **Figure 8(b)**. The linear relationship of t/q_t versus t, based on the PSO kinetic model, fits the kinetic data well, as indicated in **Table 1**, with a very high regression coefficient close to unity (R^2 = 1) for sample CuFNPs (4) and equal to (R^2 = 1) for sample CuFNPs (5). This suggests that dye adsorption onto the adsorbent involves chemical bonding between the adsorbate and the functional groups on the adsorbent's

surface. This material's adsorption capacity is substantially enhanced by these chemical interactions. At equilibrium, the equilibrium adsorption is impacted by the quantity of adsorbate on the adsorbent's surface and the quantity adsorbed.

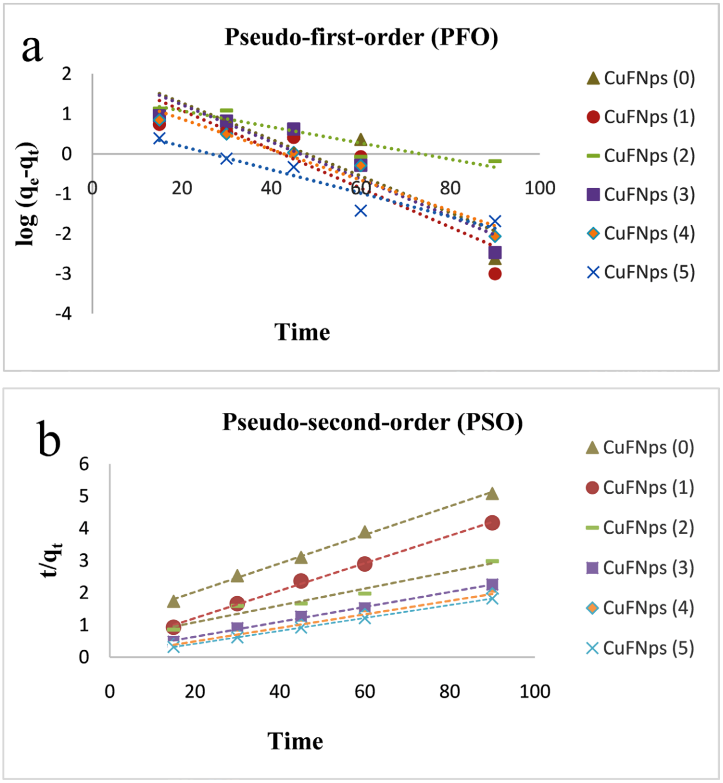

Figure 8. Pseudo (a) first-order and (b) second-order kinetic plots for the adsorption of AYR dye onto CuFNP samples.

Table 1. Kinetic parameters for the adsorption of AYR onto CuFNP samples.

Samples	$q_{e\,exp}$ (mg/g)	Lagergren pseudo-first-order model			Pseudo-second-order model		
		q_{e1}	k_1	R^2	q_{e2}	k_2	R^2
CuFNPs (0)	17.8	0.99	−0.0051	0.698	22.52	0.0444	0.9969
CuFNPs (1)	21.6	0.95	−0.0488	0.8207	23.42	0.0427	0.9976
CuFNPs (2)	30.2	0.98	−0.0202	0.8783	38.17	0.0262	0.9567
CuFNPs (3)	39.9	0.95	−0.0466	0.8915	43.29	0.0231	0.9968
CuFNPs (4)	45.8	0.96	−0.0382	0.9492	47.62	0.021	0.9999
CuFNPs (5)	49.4	0.97	−0.0293	0.9128	50	0.02	1

3.6. Adsorption Isotherm

Adsorption isotherms are used to evaluate the efficacy of an adsorbent in removing specific contaminants and to better understand the adsorption mechanism.

They demonstrate the equilibrium relationship between the adsorbent and the adsorbate [38]. Langmuir and Freundlich models are frequently implemented to approximate equilibrium adsorption data among the numerous adsorption isotherm models.

The Langmuir model suggests that the adsorbate molecules do not interact intermolecularly, and the pigment is adsorbed in a monolayer on the adsorbent's surface. Equation (8) illustrates this in its linear form. The linear plot of the Langmuir isotherm is depicted in **Figure 9(a)**.

$$q_e = \frac{q_{\max} k_L C_e}{1 + k_L C_e}, \tag{8}$$

where k_L is the Langmuir constant, q_m represents the maximum adsorption capacity, and n denotes the adsorption intensity.

The relevant Langmuir parameters and correlation coefficients are provided in **Table 2**. The slope of $(1/q_{\max})$ and the intercept of $(1/k_L)$ are obtained from **Figure 9(a)**. To predict the efficiency of adsorption, the key features of the Langmuir isotherm are described using a dimensionless constant known as the separation factor, or equilibrium parameter R_L. This parameter sheds light on the attraction between the adsorbate and the adsorbent and is expressed by the following equation (9):

$$R_L = \frac{1}{1 + k_L C_0}, \tag{9}$$

where C_0 (mg/g) represents the amount of dye adsorbed per unit mass at equilibrium, and k_L is the Langmuir constant.

The following **Table 2** shows the values of R_L. The R_L values for AYR dye were more than zero and less than unity, indicating good adsorption. Furthermore, it was found that R_L values decrease as the initial concentration increases, suggesting that AYR dye adsorption becomes more favorable. The adsorption process follows the Langmuir adsorption isotherm. This means that the surface is homogeneous, all sites are energetically equivalent, and the energy of adsorption is equal for all sites. The process involves monolayer coverage only, without interactions between adsorbate molecules on neighboring sites. The Freundlich adsorption isotherm equation was applied to AYR dye. The linear form of the Freundlich isotherm can be represented by an equation (10).

$$\log q_e = \log k_f + \frac{1}{n} \log C_e, \tag{10}$$

where k_f represents the Freundlich constants, q_m is the maximum adsorption capacity, and n indicates the adsorption intensity.

The plot of $\log q_e$ against $\log C_e$ gives the constants $\frac{1}{n}$ and k_f, corresponding to the slope and intercept, respectively, as shown in **Figure 9(b)**. The corresponding Freundlich parameters and correlation coefficient are reported in **Table 2**. The Langmuir model provides a significantly better fit for the experimental equilibrium

adsorption data of AYR dye on the surface compared to the Freundlich model, as indicated by a higher R^2 value. The kinetic study shows that the process is controlled by the chemisorption step. This is evident because AYR dye, an azo dye containing N = N with an electron cloud, has functional groups that acquire a negative charge. These characteristics allow the addition of ferrite molecules, providing the composite with an active center, due to the presence of Fe^{2+} and Fe^{3+}, which can serve as centers for chemical bonding between the dye and the composite.

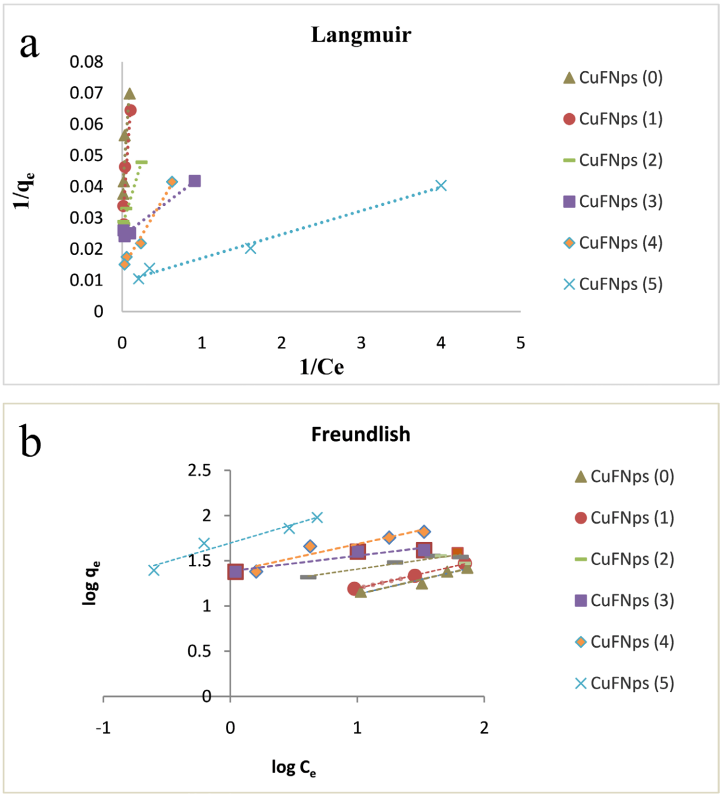

Figure 9. Adsorption isotherms of AYR dye on CuFNPs using (a) Langmuir and (b) Freundlich models.

Table 2. Determination of Langmuir and Freundlich parameters for the adsorption of AYR dye onto CuFNPs samples.

Samples	Langmuir isotherm			Freundlich isotherm		
	k_L (mg/g)	R_L	R^2	k_F (mg/g)	n	R^2
CuFNPs (0)	4.01	0.004963	0.8575	0.3036	6.79	0.9328
CuFNPs (1)	1.86	0.010638	0.9447	0.3819	6.4	0.9455
CuFNPs (2)	3.15	0.006309	0.9818	0.9462	16.15	0.9475
CuFNPs (3)	1.74	0.011364	0.984	0.7806	25.43	0.7807
CuFNPs (4)	2.06	0.009615	0.9829	0.3069	23.87	0.8833
CuFNPs (5)	0.8	0.02439	0.9891	0.4145	49.64	0.9446

3.7. Biological Activity Study

The antibacterial activities of CuFNPs samples were evaluated against four bacterial strains, including both gram-positive and gram-negative bacteria, as well as pathogenic yeast. The antibacterial findings are presented in Figure 10 and Table 3. In this experiment, CuFNPs (5) demonstrated exceptional antimicrobial efficacy against B. cereus and S. aureus, with inhibition zones of 39.0 to 41.0 mm, and were also effective against P. aeruginosa and E. coli, showing inhibition zones of 43.0 mm and 37.0 mm, respectively. Additionally, it exhibited broad-spectrum activity against the yeast Candida albicans, with a 37.0 mm inhibition zone. This effectiveness is attributed to the disruption of the cell membrane structure and the inhibition of the budding process [39]. On the other hand, based on SEM results, the nanosize of CuFNPs contributes to providing a higher surface area, leading to better contact. In contrast, CuFNPs samples (1) to (4) showed lower activity against *B. cereus* and *S. aureus*, with inhibition zones ranging from 16.0 to 26.0 mm, and lacked efficacy against the pathogenic yeast *C. albicans*. Furthermore, CuFNPs (1) and (2) exhibited antibacterial activity primarily against gram-positive and gram-negative bacteria. Overall, CuFNPs (5) is identified as the most promising antimicrobial agent among the tested samples. The mode of action for CuFNPs (5) involves inhibiting the bacterial cell wall's mucopolysaccharide component, peptidoglycan, and includes various actions contributing to its bactericidal effect [40]. These actions include inhibition of cell wall biosynthesis, protein biosynthesis, membrane disruption, nucleic acid synthesis inhibition, mycobacterial ATP synthase inhibition, direct interaction with PBPs, inhibition of transpeptidase activity, binding to the peptide chain of peptidoglycan subunits, blocking transglycosylation and transpeptidation, and blocking transport of peptidoglycan subunits across the cytoplasmic membrane.

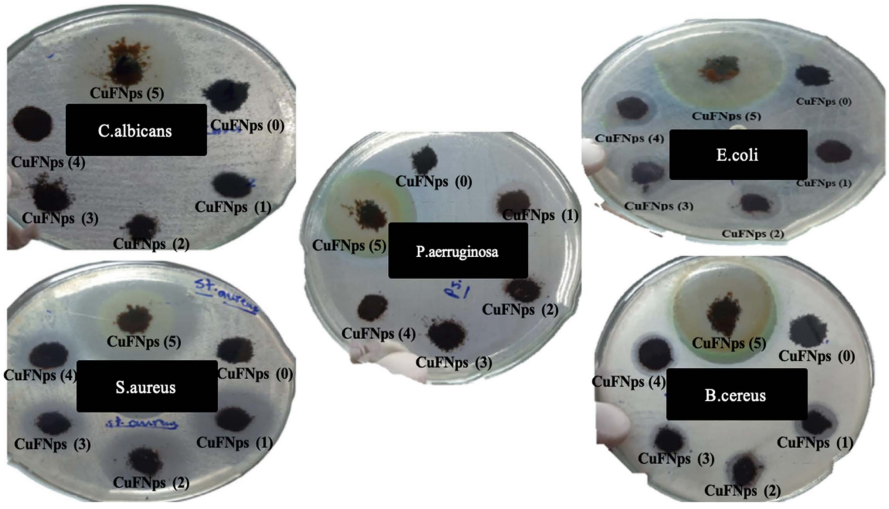

Figure 10. Images of the seeded plates for the tested microbes, treated with the prepared samples after incubation at 37˚C for 24 hours.

Table 3. Diameter of the inhibition zones (in millimeters) for the samples.

Test bacteria \ Samples	CuFNPs (0)	CuFNPs (1)	CuFNPs (2)	CuFNPs (3)	CuFNPs (4)	CuFNPs (5)	*CN
E. coli	NiL	23.0	18.0	17.0	18.0	43.0	15.0
P. aeruginosa	NiL	17.0	13.0	NiL	NiL	37.0	16.0
B. cereus	NiL	16.0	15.0	15.0	18.0	41.0	19.0
S. aureus	NiL	26.0	23.0	20.0	21.0	39.0	24.0
C. albicans	NiL	NiL	NiL	NiL	NiL	31.0	-

NiL: No antimicrobial activity recoded; *CN: Gentamycin standard antibiotic disc (10.0 mcg).

4. Conclusion

CuFNPs were successfully synthesized using two simple methods: co-precipitation and microwave-assisted synthesis. The samples were analyzed using XRD, SEM, and VSM. X-ray analysis indicated crystallite diameters ranging from 24 to 31 nm. SEM images showed multigrain aggregation of small particles. The adsorption capacity of CuFNPs was assessed for AYR dye removal from aqueous solutions under various conditions using UV-Vis. The equilibrium adsorption data fitted well with Langmuir isotherms and the PSO kinetic model. The study also evaluated the efficiency of the microwave-assisted method over the co-precipitation technique for AYR dye removal. CuFNPs (5) demonstrated the best removal efficiency compared to the other samples. Also, the $CuFe_2O_4$ hysteresis curve showed superparamagnetic material with no saturation magnetization (Ms). The antibacterial activities of CuFNPs samples were assessed against four bacterial strains, including gram-negative and gram-positive bacteria, as well as pathogenic yeast. CuFNPs (5) showed the most promising antimicrobial activity among the tested samples. It would be worthwhile to further investigate the mechanism of action of the produced nano-ferrites during adsorption and the sites that interact with the dye. Similarly, studying the interaction between the nano-ferrites and the pathogenic species could be achieved by introducing different characterization techniques to track the adsorption processes.

Acknowledgements

The authors extend their appreciation to the University of Jeddah for the facilities provided.

Conflicts of Interest

The authors declare no conflicts of interest regarding the publication of this paper.

References

[1] Abdulrazzak, I.A., Bierk, H. and Abdulrazzaq, A.A. (2020) Monitoring and Evaluation of the Water Pollution. *IOP Conference Series*: *Materials Science and*

Engineering, **881**, Article ID: 012101.
https://doi.org/10.1088/1757-899x/881/1/012101

[2] Jabeen, A., Huang, X. and Aamir, M. (2015) The Challenges of Water Pollution, Threat to Public Health, Flaws of Water Laws and Policies in Pakistan. *Journal of Water Resource and Protection*, **7**, 1516-1526.
https://doi.org/10.4236/jwarp.2015.717125

[3] Qadri, H., Ahmad, R., Mohammad, B., Mehmood, A. and Hamid, G. (2020) Fresh Water Pollution Dynamics and Remediation. Springer.
https://doi.org/10.1007/978-981-13-8277-2

[4] Sanda, B.Y. and Ibrahim, I. (2020) Causes, Categories and Control of Water Pollution. *International Journal of Scientific Engineering and Science*, **4**, 84-90.

[5] Hao, O.J., Kim, H. and Chiang, P. (2000) Decolorization of Wastewater. *Critical Reviews in Environmental Science and Technology*, **30**, 449-505.
https://doi.org/10.1080/10643380091184237

[6] Katheresan, V., Kansedo, J. and Lau, S.Y. (2018) Efficiency of Various Recent Wastewater Dye Removal Methods: A Review. *Journal of Environmental Chemical Engineering*, **6**, 4676-4697. https://doi.org/10.1016/j.jece.2018.06.060

[7] Reddy, D.H.K. and Yun, Y. (2016) Spinel Ferrite Magnetic Adsorbents: Alternative Future Materials for Water Purification? *Coordination Chemistry Reviews*, **315**, 90-111. https://doi.org/10.1016/j.ccr.2016.01.012

[8] Vinosha, P.A., Manikandan, A., Judith Ceicilia, A.S., Dinesh, A., Francisco Nirmala, G., Preetha, A.C., *et al*. (2021) Review on Recent Advances of Zinc Substituted Cobalt Ferrite Nanoparticles: Synthesis Characterization and Diverse Applications. *Ceramics International*, **47**, 10512-10535. https://doi.org/10.1016/j.ceramint.2020.12.289

[9] Amiri, M., Salavati-Niasari, M. and Akbari, A. (2019) Magnetic Nanocarriers: Evolution of Spinel Ferrites for Medical Applications. *Advances in Colloid and Interface Science*, **265**, 29-44. https://doi.org/10.1016/j.cis.2019.01.003

[10] Kumari, C. and Lahiri, P. (2019) Synthesis and Characterization of Nickel-Based Cobalt Ferrite Nanopowder. *Macromolecular Symposia*, **388**, Article ID: 1900026.
https://doi.org/10.1002/masy.201900026

[11] Kumar, A. and Gangawane, K.M. (2022) Synthesis and Effect on the Surface Morphology & Magnetic Properties of Ferrimagnetic Nanoparticles by Different Wet Chemical Synthesis Methods. *Powder Technology*, **410**, Article ID: 117867.
https://doi.org/10.1016/j.powtec.2022.117867

[12] Bhaduri, B., Dikshit, A.K., Kim, T. and Tripathi, K.M. (2022) Research Progress and Prospects of Spinel Ferrite Nanostructures for the Removal of Nitroaromatics from Wastewater. *ACS Applied Nano Materials*, **5**, 16000-16026.
https://doi.org/10.1021/acsanm.2c02684

[13] Mishra, S., Sahoo, S.S., Debnath, A.K., Muthe, K.P., Das, N. and Parhi, P. (2020) Cobalt Ferrite Nanoparticles Prepared by Microwave Hydrothermal Synthesis and Adsorption Efficiency for Organic Dyes: Isotherms, Thermodynamics and Kinetic Studies. *Advanced Powder Technology*, **31**, 4552-4562.
https://doi.org/10.1016/j.apt.2020.10.001

[14] Mogharbel, R., Tahar, L.B., Huili, H. and Grindi, B. (2023) Ultrasmall Cu-Substituted NiZn Ferrite Nanoparticles: Efficiency for the Removal of the Alizarin Red S Dye and Reusability. *Arabian Journal for Science and Engineering*, **49**, 311-337.
https://doi.org/10.1007/s13369-023-08107-x

[15] Kombaiah, K., Vijaya, J.J., Kennedy, L.J. and Bououdina, M. (2017) Optical, Magnetic

and Structural Properties of $ZnFe_2O_4$ Nanoparticles Synthesized by Conventional and Microwave Assisted Combustion Method: A Comparative Investigation. *Optik*, **129**, 57-68. https://doi.org/10.1016/j.ijleo.2016.10.058

[16] Zaharieva, K., Rives, V., Tsvetkov, M., Cherkezova-Zheleva, Z., Kunev, B., Trujillano, R., *et al*. (2015) Preparation, Characterization and Application of Nanosized Copper Ferrite Photocatalysts for Dye Degradation under UV Irradiation. *Materials Chemistry and Physics*, **160**, 271-278. https://doi.org/10.1016/j.matchemphys.2015.04.036

[17] Nithiyanantham, S. (2020) Synthesis and Characterization of Cobalt Ferrite through Co-Precipitation Technique. *Letters in Applied NanoBioScience*, **10**, 1871-1876. https://doi.org/10.33263/lianbs101.18711876

[18] Ibrahim, A.M., Munshi, G.H. and Al-Harbi, L.M. (2018) Copper(II) Oxide Nanocatalyst Preparation and Characterization: Green Chemistry Route. *Bulletin of the National Research Centre*, **42**, Article No. 6. https://doi.org/10.1186/s42269-018-0006-5

[19] da Silva, I.B.T., D'Assunção, A.G., de Oliveira, J.B.L. and de Holanda, S.M. (2019) Efficiency Estimative and Characterization of Nickel Ferrite Nanoparticles Produced by Sol-Gel Modified by ICR Cross-Linked Technique. *Materials Letters*, **254**, 13-16. https://doi.org/10.1016/j.matlet.2019.07.022

[20] Zabihi, O., Ahmadi, M., Liu, C., Mahmoodi, R., Li, Q. and Naebe, M. (2020) Development of a Low Cost and Green Microwave Assisted Approach Towards the Circular Carbon Fibre Composites. *Composites Part B*: *Engineering*, **184**, Article ID: 107750. https://doi.org/10.1016/j.compositesb.2020.107750

[21] Mannaa, M.A., Altass, H.M. and Salama, R.S. (2021) MCM-41 Grafted with Citric Acid: The Role of Carboxylic Groups in Enhancing the Synthesis of Xanthenes and Removal of Heavy Metal Ions. *Environmental Nanotechnology*, *Monitoring & Management*, **15**, Article ID: 100410. https://doi.org/10.1016/j.enmm.2020.100410

[22] Ehi-Eromosele, C.O., Olugbuyirozz, J.A.O., Taiwo, O.S., Bamgboye, O.A. and Ango, C.E. (2018) Synthesis and Evaluation of the Antimicrobial Potentials of Cobalt Doped- and Magnesium Ferrite Spinel Nanoparticles. *Bulletin of the Chemical Society of Ethiopia*, **32**, 451-458. https://doi.org/10.4314/bcse.v32i3.4

[23] El-Serwy, W.S., Mohamed, N.A., El-Serwy, W.S., Kassem, E.M.M. and Abd El Aty, A.A. (2015) Synthesis of New Benzofuran Derivatives and Evaluation of Their Antimicrobial Activities. *Research Journal of Pharmaceutical*, *Biological and Chemical Sciences*, **6**, 213-224.

[24] Mostafa, H., Pala, A., Högel, J., Hlavac, M., Dietrich, E., Westhoff, M.A., *et al*. (2016) Immune Phenotypes Predict Survival in Patients with Glioblastoma Multiforme. *Journal of Hematology & Oncology*, **9**, Article No. 77. https://doi.org/10.1186/s13045-016-0272-3

[25] Xu, J., Yang, H., Fu, W., Du, K., Sui, Y., Chen, J., *et al*. (2007) Preparation and Magnetic Properties of Magnetite Nanoparticles by Sol-Gel Method. *Journal of Magnetism and Magnetic Materials*, **309**, 307-311. https://doi.org/10.1016/j.jmmm.2006.07.037

[26] Cornell, S.E. (1999) Turkey: Return to Stability? *Middle Eastern Studies*, **35**, 209-234. https://doi.org/10.1080/00263209908701292

[27] Devan, R.S., Kolekar, Y.D. and Chougule, B.K. (2006) Effect of Cobalt Substitution on the Properties of Nickel-Copper Ferrite. *Journal of Physics*: *Condensed Matter*, **18**, 9809-9821. https://doi.org/10.1088/0953-8984/18/43/004

[28] Evans, B.J. and Hafner, S.S. (1968) Mössbauer Resonance of Fe57 in Oxidic Spinels Containing Cu and Fe. *Journal of Physics and Chemistry of Solids*, **29**, 1573-1588. https://doi.org/10.1016/0022-3697(68)90100-5

[29] Bonacchi, D., Caneschi, A., Dorignac, D., Falqui, A., Gatteschi, D., Rovai, D., *et al*. (2004) Nanosized Iron Oxide Particles Entrapped in Pseudo-Single Crystals of Γ-cyclodextrin. *Chemistry of Materials*, **16**, 2016-2020. https://doi.org/10.1021/cm034948e

[30] Ibrahim, A.M., El-Latif, M.M.A. and Mahmoud, M.M. (2010) Synthesis and Characterization of Nano-Sized Cobalt Ferrite Prepared via Polyol Method Using Conventional and Microwave Heating Techniques. *Journal of Alloys and Compounds*, **506**, 201-204. https://doi.org/10.1016/j.jallcom.2010.06.177

[31] Kuznetsov, M.V., Morozov, Y.G. and Belousova, O.V. (2013) Synthesis of Copper Ferrite Nanoparticles. *Inorganic Materials*, **49**, 606-615. https://doi.org/10.1134/s0020168513050063

[32] Narang, S.B. and Pubby, K. (2021) Nickel Spinel Ferrites: A review. *Journal of Magnetism and Magnetic Materials*, **519**, Article ID: 167163. https://doi.org/10.1016/j.jmmm.2020.167163

[33] Gouamid, M., Ouahrani, M.R. and Bensaci, M.B. (2013) Adsorption Equilibrium, Kinetics and Thermodynamics of Methylene Blue from Aqueous Solutions Using Date Palm Leaves. *Energy Procedia*, **36**, 898-907. https://doi.org/10.1016/j.egypro.2013.07.103

[34] Salleh, M.A.M., Mahmoud, D.K., Karim, W.A.W.A. and Idris, A. (2011) Cationic and Anionic Dye Adsorption by Agricultural Solid Wastes: A Comprehensive Review. *Desalination*, **280**, 1-13. https://doi.org/10.1016/j.desal.2011.07.019

[35] López-Luna, J., Ramírez-Montes, L.E., Martinez-Vargas, S., Martínez, A.I., Mijangos-Ricardez, O.F., González-Chávez, M.D.C.A., *et al*. (2019) Linear and Nonlinear Kinetic and Isotherm Adsorption Models for Arsenic Removal by Manganese Ferrite Nanoparticles. *SN Applied Sciences*, **1**, Article No. 950. https://doi.org/10.1007/s42452-019-0977-3

[36] Chairat, M., Rattanaphani, S., Bremner, J.B. and Rattanaphani, V. (2008) Adsorption Kinetic Study of Lac Dyeing on Cotton. *Dyes and Pigments*, **76**, 435-439. https://doi.org/10.1016/j.dyepig.2006.09.008

[37] Kumar, K.V. (2006) Linear and Non-Linear Regression Analysis for the Sorption Kinetics of Methylene Blue onto Activated Carbon. *Journal of Hazardous Materials*, **137**, 1538-1544. https://doi.org/10.1016/j.jhazmat.2006.04.036

[38] Ali, R.M., Hamad, H.A., Hussein, M.M. and Malash, G.F. (2016) Potential of Using Green Adsorbent of Heavy Metal Removal from Aqueous Solutions: Adsorption Kinetics, Isotherm, Thermodynamic, Mechanism and Economic Analysis. *Ecological Engineering*, **91**, 317-332. https://doi.org/10.1016/j.ecoleng.2016.03.015

[39] Kim, K., Sung, W.S., Suh, B.K., Moon, S., Choi, J., Kim, J.G., *et al*. (2008) Antifungal Activity and Mode of Action of Silver Nano-Particles on Candida Albicans. *BioMetals*, **22**, 235-242. https://doi.org/10.1007/s10534-008-9159-2

[40] Mc Dermott, P.F., Walker, R.D. and White, D.G. (2003) Antimicrobials: Modes of Action and Mechanisms of Resistance. *International Journal of Toxicology*, **22**, 135-143. https://doi.org/10.1080/10915810305089